J Appl Electrochem (2008) 38:653–662
DOI 10.1007/s10800-008-9484-8

ORIGINAL PAPER

Effect of W on PtSn/C catalysts for ethanol electrooxidation

J. Ribeiro · D. M. dos Anjos · J. -M. Léger · F. Hahn · P. Olivi · A. R. de Andrade · G. Tremiliosi-Filho · K. B. Kokoh

Received: 10 July 2007 / Revised: 8 January 2008 / Accepted: 10 January 2008 / Published online: 30 January 2008

Abstract Binary and ternary Pt-based catalysts were prepared by the Pechini–Adams modified method on carbon Vulcan XC-72, and different nominal compositions were characterized by TEM and XRD. XRD showed that the electrocatalysts consisted of the Pt displaced phase, suggesting the formation of a solid solution between the metals Pt/W and Pt/Sn. Electrochemical investigations on these different electrode materials were carried out as a function of the electrocatalyst composition, in acid medium (0.5 mol dm^{-3} H_2SO_4) and in the presence of ethanol. The results obtained at room temperature showed that the PtSnW/C catalyst display better catalytic activity for ethanol oxidation compared to PtW/C catalyst. The reaction products (acetaldehyde, acetic acid and carbon dioxide) were analyzed by HPLC and identified by *in situ* infrared reflectance spectroscopy. The latter technique also allowed identification of the intermediate and adsorbed species. The presence of linearly adsorbed CO and CO_2 indicated that the cleavage of the C–C bond in the ethanol substrate occurred during the oxidation process. At 90 °C, the $Pt_{85}Sn_8W_7$/C catalyst gave higher current and power performances as anode material in a direct ethanol fuel cell (DEFC).

Keywords PtSnW nanoparticles · Ethanol oxidation · Binary and ternary electrocatalysts · DEFC

J. Ribeiro · D. M. dos Anjos · J.-M. Léger · F. Hahn · K. B. Kokoh (✉)
Equipe Electrocatalyse, UMR 6503 CNRS, Université de Poitiers, 40 avenue du Recteur Pineau, 86022 Poitiers Cedex, France
e-mail: boniface.kokoh@univ-poitiers.fr

P. Olivi · A. R. de Andrade
Departamento de Quimica da Faculdade de Filosofia, Ciências e Letras de Ribeirão Preto, Universidade de São Paulo, Av. Bandeirantes, 3900, 14040-901 Ribeirão Preto, SP, Brazil

D. M. dos Anjos · G. Tremiliosi-Filho
Instituto de Quimica de São Carlos, Universidade de São Paulo, Caixa Postal 780, 13560-970 São Carlos, SP, Brazil

1 Introduction

There is currently a great interest in developing different kinds of fuel cells as power sources in portable devices such as cell phones, computers, cam recorders, etc. Among the various fuels that can be used in PEMFCs, ethanol is the most promising one because it is a renewable and safe molecule, and it is easy to store and handle. Moreover, ethanol has a high theoretical energy (8 kWh kg^{-1} against 6.1 kWh kg^{-1} for methanol and 33 kWh kg^{-1} for pure hydrogen without storage) [1, 2]. Based on literature data, ethanol electrooxidation on platinum encounters many problems such as deactivation of the catalyst because of the poisoning CO-species and intermediates adsorbed on Pt active sites [1–10]. In order to enhance the catalytic activity of these catalysts towards alcohol oxidation, a secondary metal is usually introduced as co-catalyst and two mechanisms have been proposed. One of them, the well-known bi-functional mechanism where different transition metals such as Ru, Re, Os, Ir, Sn, and Mo have been used to modify Pt-based electrode materials [4–6, 8–35]. Besides that at lower potentials, electronic effects also explain the enhancement of the activity Pt-based electrocatalyst [35]. PtSn catalyst is generally considered the best anode for ethanol oxidation. To further improve ethanol reactivity, we have introduced ruthenium as a third metal in the PtSn catalyst composition, which enhanced the power density from *ca.* 30 [8, 10, 19, 26, 28–34] to 50 mW cm^{-2}

[30]. A power density of 32 mW cm^{-2} when PtSnIr is used as anode has been reported [28]. So, the introduction of a third metal into the bimetallic PtSn catalysts leads to outstanding performances in DEFC operated at low temperature. Sn and/or the third metal provide O-species for CO removal from the Pt active sites during the dissociative oxidation of ethanol [8, 10, 29, 30].

The aim of this paper is to report results on the development of ternary PtSnW/C electrocatalysts prepared by thermal decomposition of a polymeric precursor (DPP) and their application in ethanol electrooxidation. Tungsten was used to promote Pt in different oxidation processes in which its oxides interacted with CO adsorbed on the Pt surface [36]. In the case of the methanol oxidation reaction (MOR), it has been assumed that WO_x operates via a bifunctional mechanism [36] or via a hydrogen spillover effect [37–39] according to the following reactions:

$$WO_3 + xPtH \rightarrow H_xWO_3 + xPt \quad (1)$$

$$H_xWO_3 \rightarrow WO_3 + xe^- + xH^+ \quad (2)$$

In these reactions, the hydrogen atoms are abstracted from CH_3OH via Pt sites and then transferred to WO_3. It has been observed that, when WO_3 is present in the catalyst, the methanol oxidation rate is higher than that obtained with pure Pt because free Pt sites are regained more quickly [37].

Umeda et al. have studied ternary PtRuW catalysts deposited on a gold substrate toward the MOR and observed a significant shift in the onset potential to lower values and a remarkable enhancement in the current density for the MOR [36]. Recently, Tanaka et al. [38] have shown that the presence of WO_x increases the electrochemical activity of the PtRu catalyst toward ethanol oxidation (EOR), with high current densities and an onset potential toward low values.

In this paper the electrochemical performance of the PtSnW/C electrocatalysts will be compared with those of PtSn and PtW/C and complete cell DEFC performance measurements will be reported to demonstrate the electrocatalytic activities of the prepared electrocatalysts.

2 Experimental

2.1 Catalysts preparation

Supported Pt-based catalysts were synthesized by thermal decomposition of a polymeric precursor (DPP) as previously described [28, 40–42]. First, the Pt and W polymeric precursors (metal–resin) were prepared separately. Then, citric acid (CA) (Merck) was mixed with ethylene glycol (EG) (Merck) at 60–65 °C. The metal precursor (H_2PtCl_6 or $WCl_6.xH_2O$ (Aldrich) 0.1 mol dm^{-3} solution dissolved in isopropanol) was then added to this mixture to give CA:EG:M molar ratios of 1:4:0.25 and 1:6:0.17 for M = Pt and M = W, respectively. After total dissolution of the precursor salt, the temperature was raised to 90 °C, and the mixture was kept under vigourous stirring for 2–3 h. The tin polymeric precursor (Sn-resin) was also prepared in a similar way, but the molar ratio CA:EG: TC was 3:10:1, where TC is tin citrate, prepared as described elsewhere [41]. Precursor mixtures were prepared for each nominal composition by dissolving the appropriate amounts of Pt-resin (2.9×10^{-4} mol of Pt/g of resin), W-resin (1.3×10^{-4} mol of W/g of resin), and Sn-resin (7.1×10^{-4} mol of Sn/g of resin). Carbon (Vulcan XC 72), which had been previously treated for 4 h at 400 °C under nitrogen atmosphere, was added to the precursor mixture, to obtain a catalyst loading of 40 wt.%. This mixture was finally dispersed in ethanol (2 mL) by ultrasonication for 10 min. Thermal treatment was carried out in a tubular oven under a nitrogen atmosphere. The temperature was firstly increased to 250 °C at a rate of 1 °C min^{-1}, and it was kept there for 1 h. Then, the temperature was increased to 300 °C at a rate of 15 °C min^{-1}, and kept there for another hour. The temperature was then increased to 400 °C at a rate of 30 °C min^{-1} and kept there for 2 h. Finally, after being cooled to room temperature, the catalysts were again kept in an oven under air atmosphere at 400 °C for 1 h to eliminate the excess organic carbon.

2.2 Catalysts physicochemical characterizations

XRD patterns of the catalysts were obtained on an X-ray diffractometer (model D5005 Brucker AXS instrument) operating with the Cu Kα radiation (λ = 1.5406 Å) generated at 40 kV and 40 mA. The following parameters were kept constant during the X-ray analysis: 2θ range = 20–90°, step = 0.03°, step time = 3 s, and total analysis time = 1.94 h. The catalyst phase composition and the analysis of the relevant position to the $K_{\alpha 1}$ monochromatic radiation were obtained by fitting the experimental angular range of interest to the pseudo-Voigt function per crystalline peak with a computer refinement program (Profile Plus Executable, Siemens AG). The crystallite size values were obtained using the Debye–Scherrer equation [43]:

$$D = \frac{K\left(\lambda \times \frac{180^\circ}{\pi}\right)}{\sqrt{\beta^2 - S^2)}\cos\theta_\beta},$$

where D is the apparent crystallite mean size, K is the shape factor (0.9 for spherical crystallite), λ is the radiation wavelength (1.5406 Å), S is the instrumental line broadening (0.001°), β is the reflection width at half-maximum intensity (FWHM), and θ_β is the angle at the maximum intensity.

A computer program using the least-squares method (U-Fit.exe v.1.3-1992) calculated the unit cell parameters. Experimental 2θ and reflection parameters (*hkl*) were used to obtain the unit cell parameters.

The electrocatalyst powder was mixed with water and ethanol and ultrasonically treated until complete ink homogenization was achieved. The morphology of the different electrocatalyst inks was then examined by Transmission Electron Microscopy (TEM) using a Philips CM 120 microscope equipped with a LaB_6 filament. Energy dispersive X-ray analysis (EDX) using a Leica-Zeiss LEO 440 model SEM coupled to an Oxford 7060 model analyzer also allowed us to estimate the nanoparticles compositions.

2.3 Electrochemical measurements

For the electrochemical measurements, 2 mg of the electrocatalysts were dispersed in a solution (100 μL) containing ethanol (95 μL) and Nafion® (5 μL) (5 wt.% in aliphatic alcohol, Aldrich). The resulting ink was ultrasonically homogenized for 10 min. After homogenization, the ink was deposited onto vitreous carbon previously polished with alumina (0.3 μm) to a mirror-finish and then dried in an oven at 75 °C for 10 min.

Electrochemical measurements were carried out in a conventional three-electrode cell (30 mL) with an Autolab potentiostat (PGSTAT30). A reversible hydrogen electrode (RHE) and a slab of vitreous carbon with 4 cm^2 geometric surface area were used as reference and counter electrode, respectively. The anode potential was taken versus the reference electrode, which was separated from the solution by a Luggin–Haber capillary tip. The activity of the catalysts was evaluated by cyclic voltammetry (CV, recorded in the 0.05–1.2 V vs. RHE potential range, in 0.5 mol dm^{-3} H_2SO_4 (Aldrich) or 0.5 mol dm^{-3} H_2SO_4 + 1.0 mol dm^{-3} ethanol (Normapur) solution) and chronoamperometry at 400 mV for 2 h.

The reaction products were analyzed by High Performance Liquid Chromatography (HPLC); the equipment contained a refractive index detector. The products were separated by an Aminex HPX−87H (Bio-Rad) column using isocratic elution with sulfuric acid 1 mmol dm^{-3} at a 0.6 cm^3 min^{-1} flow rate. During the electrolysis, the evolved carbon dioxide was trapped with 1.0 mol dm^{-3} NaOH (1 mL). At the end of the experiment, nitrogen was bubbled for 15 min in the cell to remove all the CO_2 toward the trap cell. Carbonate was quantitatively analyzed by comparison with a Na_2CO_3 reference prepared under the same conditions.

The solutions were prepared with Milli-Q water (18.2 MΩ cm at 20 °C). The electrolyte solution was purged with nitrogen (U quality) prior to the measurements, in order to expel oxygen. Nitrogen was also used to maintain an inert atmosphere over the solutions during the measurements.

2.4 IR spectroscopic measurements

Ten microliters of the catalyst ink (solution content = 1 mg of catalyst + 275 μL ethanol + 15 μL Nafion®) were deposited onto a gold substrate previously polished with alumina (0.3 μm) to a mirror-finish in order to obtain a better reflectivity, and then dried in an oven at 75 °C for 5 min. IR reflectance spectra were recorded on a Bruker IFV 66v spectrometer with data acquisition techniques, that allowed us to perform Single Potential Alteration Infrared Reflectance Spectroscopy (SPAIRS) and Subtractively Normalized Interfacial Fourier Transform Infrared Reflectance Spectroscopy (SNIFTIRS) experiments. For SPAIRS, the reflectivities were recorded at 50 mV intervals during the first voltammetric scan at a low sweep rate (1 mV s^{-1}). For SNIFTIRS, the reflectivities were recorded at two different potentials, E_1 and E_2. All the potential range used in this work (0.05 and 0.6 V vs. RHE) was studied keeping the difference (E_2-E_1) constant (0.2 V).

2.5 Preparation of the catalysts and the membrane/electrode assemblies (MEAs)

The membrane electrode assemblies (MEAs) were prepared by hot pressing a pretreated Nafion® 117 membrane placed between an E-TEK cathode (1 mg cm^{-2} metal loading 40 wt.%) and a homemade anode (1 mg cm^{-2} metal loading 40 wt.%) at 125 °C for 90 s under a pressure of 35 kg cm^{-2}. The operating fuel cell performances were determined in a single DEFC with an electrode geometric surface area of 4.62 cm^2, using a Globe Tech test bench. The temperature was set to 90 °C for the fuel cell and 95 °C for the oxygen humidifier. The ethanol and oxygen pressures were set to 1 and 3 bar, respectively. The E versus i and P versus i curves were recorded using a high power potentiostat (Wenking model HP 88) interfaced with a PC.

3 Results and discussion

3.1 Catalysts physicochemical characterizations

EDX results for all the prepared electrocatalysts are presented in Table 1. These results indicate that each metal is present in an average composition close to the nominal

Table 1 XRD results and EDX analysis for different Pt-based/C electrocatalysts prepared by the DPP process

Electrocatalyst		Phase	a/Å	V/Å^3	D/nm			
Nominal	Experimental[a]				(111)	(200)	(220)	(311)
$Pt_{90}W_{10}$	$Pt_{88}W_{12}$	Pt	3.910	59.78	13.0	12.2	12.5	12.5
$Pt_{85}Sn_{15}$	$Pt_{78}Sn_{22}$	Pt	3.923	60.41	9.7	8.3	7.4	7.8
		Pt_3Sn	3.993	63.66	16.6	13.8	11.9	11.0
$Pt_{90}Sn_5W_5$	$Pt_{85}Sn_8W_7$	Pt	3.918	60.13	11.4	9.6	9.3	8.6
$Pt_{80}Sn_{15}W_5$	$Pt_{68}Sn_{24}W_8$	Pt	3.931	60.75	9.4	8.7	7.8	7.8
		Pt_3Sn	3.985	63.30	11.5	10.2	10.4	9.4
$Pt_{65}Sn_{25}W_{10}$	$Pt_{62}Sn_{23}W_{15}$	Pt	3.921	60.27	6.4	5.8	5.3	7.5
		Pt_3Sn	3.971	62.63	11.2	9.3	9.1	7.9

[a] Experimental data obtained by EDX

Data: $a_{Pt} = 3.920$ Å and $a_{Pt3Sn} = 4.001$ Å [44]

values, except the $Pt_{68}Sn_{24}W_8$/C catalyst, where the Pt content decreases far from the nominal one. At the same time the Sn amount increases in this ternary composition. Consequently, the experimental compositions of the catalysts are used.

Moreover, analysis of the electrocatalysts revealed heterogeneity in some regions. For example, the binary $Pt_{88}W_{12}$/C electrocatalyst presents Pt-rich and other W-rich regions. The Pt-rich regions are composed of large agglomerates and the W-rich regions comprise small particles (4–8 nm), as shown in Fig. 1a and d. The binary $Pt_{78}Sn_{22}$/C electrocatalyst has large particles with compositions close to $Pt_{75}Sn_{25}$ (maybe Pt_3Sn) and also small particles with compositions $Pt_{65}Sn_{35}$. The average particle size is 5.0 ± 1.8 nm. The ternary $Pt_{62}Sn_{23}W_{15}$/C electrocatalysts have the smallest particle size (3.9 ± 2.2 nm).

Figure 2 shows the XRD patterns of the carbon-supported binary PtW and PtSn and ternary PtSnW catalysts. The main characteristic peaks of the face-centred cubic (fcc) crystalline Pt (space group Fm–3m) [44] appear in all the patterns, which shows that all the electrocatalysts resemble the phase disordered structure (solid solution), with reflection planes (111), (200), (220), (311), and (222), as previously observed [28]. Figure 2 shows a slight shift in Pt peak positions for the catalysts containing Sn, which are shifted to lower 2θ values when compared with the pure Pt XRD pattern. Moreover, the binary PtSn and ternary PtSnW electrocatalysts have separate phases. The new f phase has characteristic peaks attributed to cubic Pt_3Sn (space group Pm3m) with (111), (200), (220), (311), and (222) planes [44]. We observed a similar behavior in a previous investigation with PtSnIr/C electrocatalysts [28]. Despite the difference in the atomic radius of the two metals around 4% (145 pm for Sn and 139 pm for Pt) [45], low miscibility (10%) is observed. In fact, this behavior is expected since Sn and Pt show distinct structures (tetragonal for Sn and face-centered cubic for Pt) plus different electronegativities (1.96 and 2.28/Pauling units, respectively). The large difference in electronegativity leads to the formation of the new compound (Pt_3Sn) due to a difference in electron affinity (Pt = 205.7 kJ mol^{-1} and Sn = 107.3 kJ mol^{-1}). Even though all the Hume-Rothery conditions [46] are not adequately satisfied for the formation of a substitutional solid solution, an interstitial one can be formed at a lower extension. Indeed, the fcc structure has two interstitial sites: octahedral (large) and tetrahedral (small), where the ratio between the radius of the octahedral interstice (r_o) and the atomic radius of reticule (R) for the fcc is: $r_o/R = [2 - (2)^{1/2}]/(2)^{1/2} = 0.4142$ and for the tetrahedral interstice (r_t): $r_t/R = 0.223$. In the Pt fcc structure, the closest Pt–Pt separation is 277.5 pm, which implies a platinum metallic radius of 1.39 Å. Therefore, the large spheres contained in the octahedral and tetrahedral interstices have radii 0.57 and 0.31 Å, respectively. Taking into account the Sn(0) atomic radius (1.45 Å) one can infer that Sn atoms could form a substitutional solid solution.

Unlike the prior observations regarding the PtSn/C catalyst, the introduction of W in the binary $Pt_{88}W_{12}$/C catalyst results in a slight shift of the diffraction peaks of Pt to higher 2θ-values. This suggests that there is also formation of a solid solution between Pt and W. Although there is a difference in the structure (W metallic—(bcc) body-centered cubic—and space group Im−3m), an interstitial solid solution can be formed. There is no formation of a new phase attributable to PtW. This is in agreement with electronegativity data (for W−2.36/Pauling units), which are close to those of Pt. Meanwhile, the signals related to WO_3 can be distinguished in the XRD pattern (between $20° < 2\theta < 35°$) obtained for the binary $Pt_{88}W_{12}$/C and ternary $Pt_{62}Sn_{23}W_{15}$/C catalysts. The WO_3 phase has characteristic peaks attributable to monoclinic WO_3 (space group P21/a), with (001), (020), (200), (111), and (201) planes [44]. The presence of WO_x in the ternary $Pt_{68}Sn_{24}W_8$/C and $Pt_{90}Sn_5W_5$/C catalysts is not observed in the XRD pattern. However, their presence cannot be ruled out because they may be present in small amounts and in amorphous forms. This can again be understood in terms of the coexistence of the Pt particles closer to the WO_x particles.

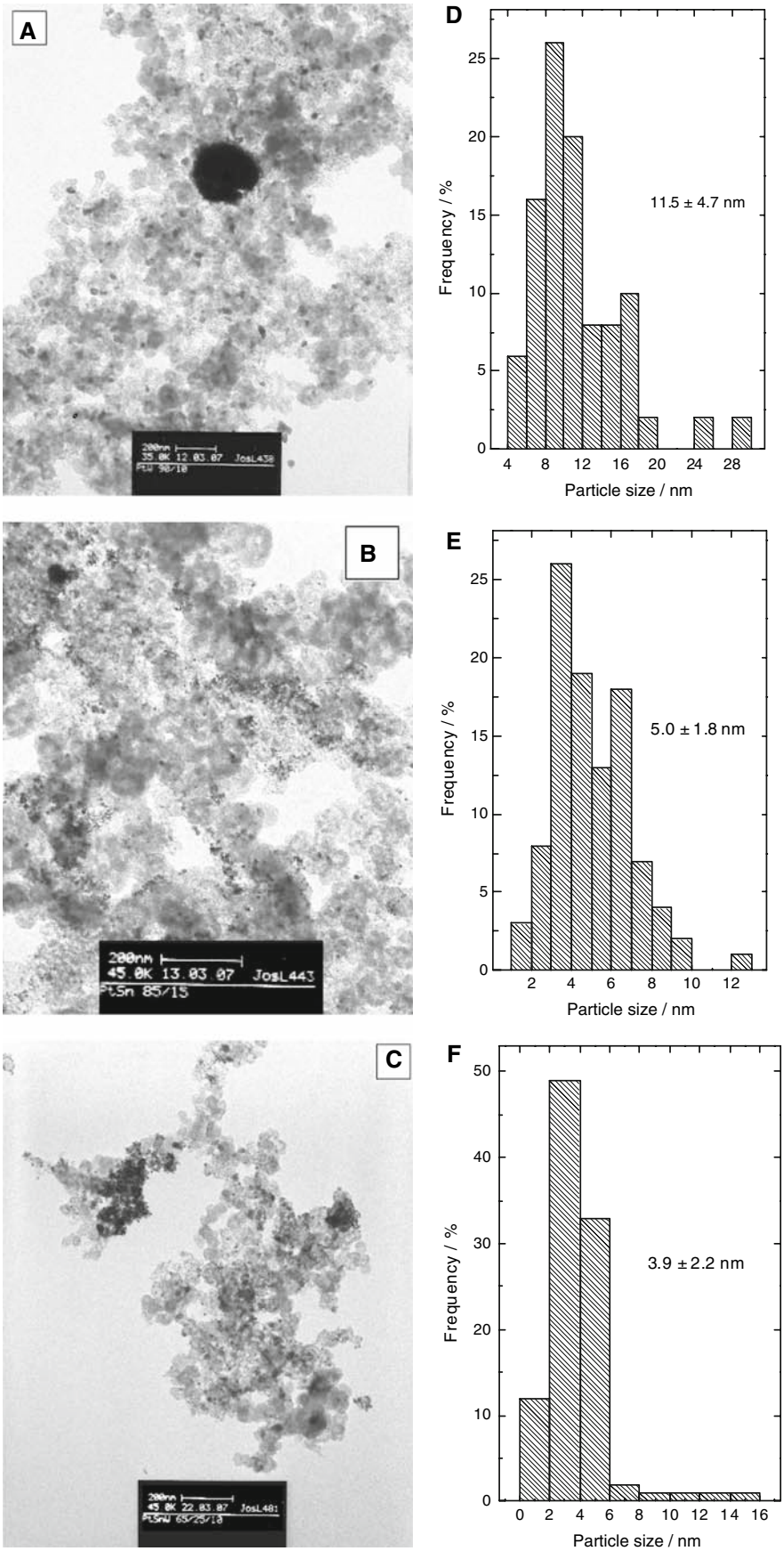

Fig. 1 (**a**), (**b**) and (**c**) TEM images and (**d**), (**e**) and (**f**) histograms of particle size distributions of Pt-based/C catalysts prepared by the DPP process. (**a**) and (**d**) $Pt_{88}W_{12}$/C; (**b**) and (**e**) $Pt_{78}Sn_{22}$/C; (**c**) and (**f**) $Pt_{62}Sn_{23}W_{15}$/C

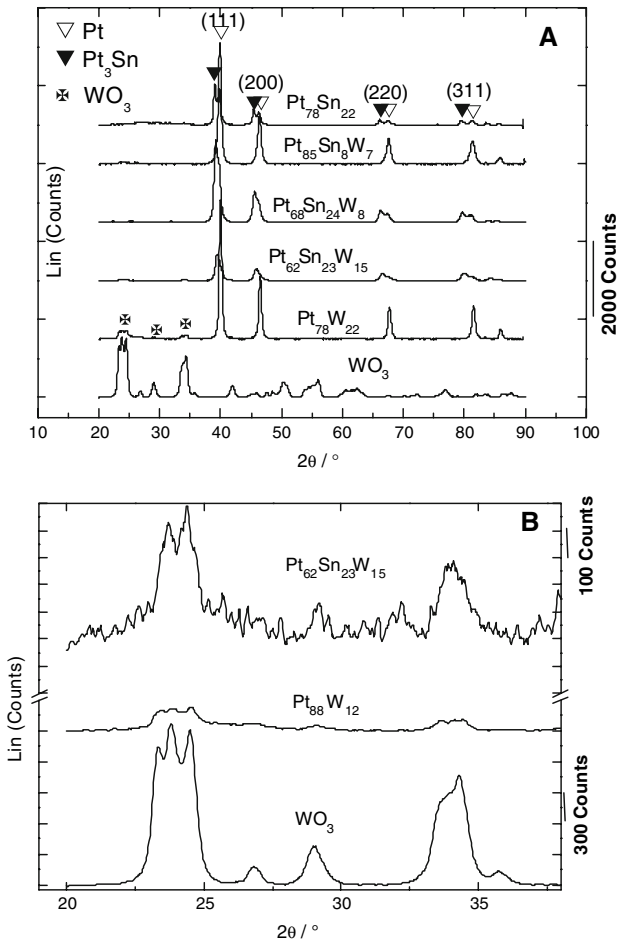

Fig. 2 XRD patterns of Pt-based catalysts prepared by the DPP process. (**a**) binary PtW, PtSn and ternary PtSnW catalysts. (**b**) Detailed WO_3 peaks

Deconvolution of the peaks in the XRD of the Pt-based catalysts was performed as described elsewhere [47] and the results (lattice parameter, cell volume, and apparent mean crystallite size, *D*) are shown in Table 1. The presence of W in the binary PtW catalyst promotes a decrease in the lattice parameter for the Pt fcc structure. In the case of the ternary PtSnW/C catalysts, the increase in the amounts of W also promotes a decrease in the lattice parameter as much for Pt as for the Pt_3Sn phases (from 3.931 to 3.921 Å and from 3.985 to 3.971 Å, respectively). On the other hand, the presence of Sn in both the binary and ternary catalysts leads to an increase in the lattice parameter (from 3.918 Å to 3.931 Å), suggesting that there is a straight dependence of the lattice parameter on Sn atom%, which follows Vegard's law [48]. Moreover, the increase in that parameter is evidence that Sn atoms are incorporated by Pt clusters which favors lattice expansion.

An apparent crystallite mean size, *D*, close to 13 nm was obtained for the Pt and Pt_3Sn phases in the binary catalysts. However, both phases of the ternary PtSnW/C catalysts have *D* values close to 9 nm, except for the Pt phase in the $Pt_{62}Sn_{23}W_{15}$/C, which has a *D* value close to 6 nm. These results are not in agreement with the TEM-data. This behavior can be explained by the fact that XRD data exhibit well-defined crystalline particles, but not amorphous ones. As a result, the average particle size is slightly displaced from those obtained by TEM.

3.2 Electrochemical characterizations

Typical CV curves obtained for the different electrocatalysts deposited on vitreous carbon in 0.5 M H_2SO_4 are shown in Fig. 3a. The voltammograms do not display well-defined hydrogen adsorption/desorption regions (0.0–0.4 V vs. RHE), and the currents in the double layer region between 0.4 and 0.85 V vs. RHE are large. This behavior is characteristic of carbon supported binary and ternary electrocatalysts containing transition metals [28, 49]. Comparing the binary and ternary electrocatalysts, one can observe that the introduction of W into binary PtSn/C favors an enhancement of the voltammetric charge.

Fig. 3b shows the representative cyclic voltammograms obtained with different electrocatalysts ($Pt_{88}W_{12}$/C, $Pt_{85}Sn_8W_7$/C and $Pt_{62}Sn_{23}W_{15}$/C) deposited on vitreous carbon in the presence of 1 M ethanol. Among the bimetallic catalyst, Sn is the best co-catalyst in the promotion of the activity of Platinum in comparison with W. For ethanol electrooxidation on binary PtSn/C, PtW/C and ternary PtSnW/C, the appearance of two peaks during the positive-going scan can be ascribed to the oxidation of the ethanol as follows [8, 10, 35, 50]:

At low potential (<0.4 V) hydrogen abstraction from ethanol competes with the dissociative adsorption on Pt surface leading to acetaldehyde and CO as the main products:

$$CH_3CH_2OH_{bulk} \rightarrow CH_3CH_2OH_{ads(Pt)} \quad (3)$$

$$CH_3CH_2OH_{ads(Pt)} \rightarrow CH_3CHOH_{ads(Pt)} + H^+ + e^- \quad (4)$$

$$CH_3CHOH_{ads(Pt)} \rightarrow CH_3CHO_{ads(Pt)} + H^+ + e^- \quad (5)$$

$$CH_3CHO_{ads(Pt)} \rightarrow CH_3CHO_{bulk} \quad (6)$$

$$CH_3CH_2OH_{ads(Pt)} \rightarrow CO + CH_x \quad (7)$$

At higher potentials (>0.4 V) the mechanism can be explained from Eqs. 8–11 i.e. interfacial water activation occurs resulting OH-species which facilitate the formation of high oxidation state compounds (acetic acid, CO_2). The addition of a co-catalyst shifts the water oxidation potential from 0.60 V vs. RHE on the single platinum surface [51] to 0.30 V vs. RHE and 0.55 V vs. RHE respectively to PtSn [36] and PtW [36]. Based on the work of Shao and Adzic [7] we cannot rule out the direct oxidation of adsorbed ethanol to form acetic acid.

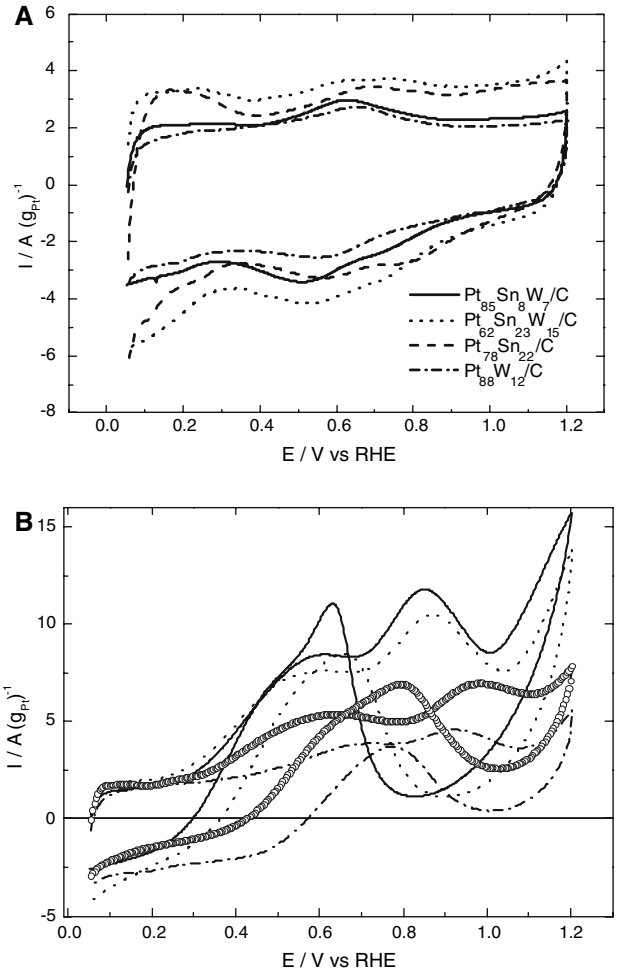

Fig. 3 Cyclic voltammograms for the 40 wt.% Pt-based/C electrodes in: (**a**) N_2-purged 0.5 mol dm^{-3} H_2SO_4 electrolyte at 20 mV s^{-1} and (**b**) –o– $Pt_{78}Sn_{22}$/C; – - – $Pt_{88}W_{12}$/C; - - - $Pt_{62}Sn_{23}W_{15}$/C and — $Pt_{85}Sn_8W_7$/C electrodes in N_2-purged 0.5 mol dm^{-3} H_2SO_4 + 1.0 mol dm^{-3} ethanol electrolyte at 20 mV s^{-1}. Current values are normalized by the Pt loading

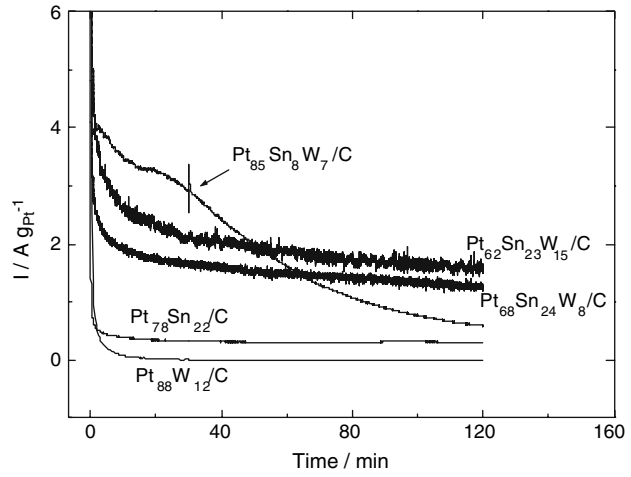

Fig. 4 Current vs. time plots for the electrooxidation of 1.0 mol dm^{-3} ethanol in 0.5 M H_2SO_4 at 0.4 V vs. RHE on various Pt-based/C catalysts. Current values are normalized by the Pt loading

$$H_2O_{(M)} \rightarrow OH_{ads(M)} + H^+ + e^- \quad (8)$$

$$CH_3CHO_{ads(Pt)} + OH_{ads(M)} \rightarrow CH_3COOH_{ads(Pt)} + H^+ + e^- \quad (9)$$

$$CH_3COOH_{ads(Pt)} \rightarrow CH_3COOH_{bulk} \quad (10)$$

$$CO_{ads(Pt)} + OH_{ads(M)} \rightarrow CO_2 + H^+ + e^- \quad (11)$$

Chronoamperometry (CA) experiments were carried out at 400 mV for 2 h, to evaluate both the electrocatalytic activity of the electrocatalysts in steady state conditions and the poisoning of the active surface. Figure 4 shows the representative chronoamperograms obtained for different catalysts whose currents were normalized by the Pt content. There is a sharp decrease in the current density during the first minutes, followed by a slow decrease over longer periods. Firstly, the active sites are free of adsorbed ethanol molecules (fast kinetic rate reaction); after that, the adsorption of new ethanol molecules is a function of the liberation of the active sites by ethanol oxidation or intermediate species, such as CO, CH_x, CH_3CHO and CH_3COOH, formed during the first minutes (rate-determining step), which are responsible for poisoning of the catalytic sites. Indeed, the ethanol oxidation reaction at Pt and PtW/C electrocatalyst is hinded compared with tin-based catalysts. For instance, $Pt_{85}Sn_8W_7$/C electrocatalyst consumes 9.3 C compared to 0.36 C at PtW/C. It can also be observed that the steady state is not reached because of the surface instability of the nanoparticles due to agglomeration and/or re-crystallization of particles during the operation. Consequently, these processes decrease the number of active sites on the surface. This behavior, particularly observed in the $Pt_{85}Sn_8W_7$/C catalyst, shows that Sn atoms are bonded more strongly into the lattice of Pt metal, as would be expected in an alloy. This is in agreement with XRD results, which show that the Sn and W atoms are incorporated by Pt clusters.

The ternary PtSnW/C electrocatalysts give better results than the binary PtSn/C and PtW/C electrocatalysts. The better activity obtained for the ternary electrocatalysts can be explained by the beneficial synergistic effect between PtSn and tungsten.

At the end of the CA, the electrolytic solution was analyzed by HPLC and the results are shown in Table 2. Acetaldehyde and acetic acid were mainly produced during electrolyzes on the ternary PtSnW/C electrocatalysts; traces of acetaldehyde were only observed for binary PtW/C. The presence of CO_2 was also detected (from 0.01 to 0.3 mM), which shows that ethanol oxidation on these catalysts results in reaction products from the cleavage of the C–C bond. However, the potential used for the CA experiment is slightly

Table 2 Results of ethanol electrolysis by different Pt-based/C electrocatalysts prepared by the DPP process

Electrocatalyst	Ethanol consumed	Ethanol crossover	Acetaldehyde	Acetic Acid	CO_2
$Pt_{88}W_{12}/C$	1.3 mM	1.1 mM	0.0 mM	0.0 mM	0.01 mM
		84.6%	trace	0.0 %	2.5 %
$Pt_{78}Sn_{22}/C$	5.7 mM	2.0 mM	2.4 mM	1.0	0.3 mM
			63.4 %	27.6 %	2.8 %
$Pt_{85}Sn_8W_7/C$[a]	7.1 mM	1.9 mM	3.8 mM	0.9 mM	0.3 mM
			73.1 %	17.3 %	2.9 %
$Pt_{68}Sn_{24}W_8/C$	5.7 mM	2.7 mM	1.8 mM	0.8 mM	0.3 mM
			56.7 %	26.7 %	1.0 %
$Pt_{62}Sn_{23}W_{15}/C$[a]	6.1 mM	2.5 mM	1.7 mM	1.5 mM	0.2 mM
			47.2 %	41.7 %	2.8 %

[a] Traces of formic acid are observed

higher (400 mV vs. RHE). In this condition, the production of acetaldehyde and acid acetic is favored.

Figure 5a shows the representative SPAIR spectra obtained for ethanol oxidation on $Pt_{62}Sn_{23}W_{15}/Au$. These spectra taken in the 1,000–3,000 cm^{-1} spectral range and for potentials between 100 and 1,200 mV vs. RHE were recorded at 50 mV intervals during a cyclic voltammetric experiment performed at 1 mV s^{-1}. The band at

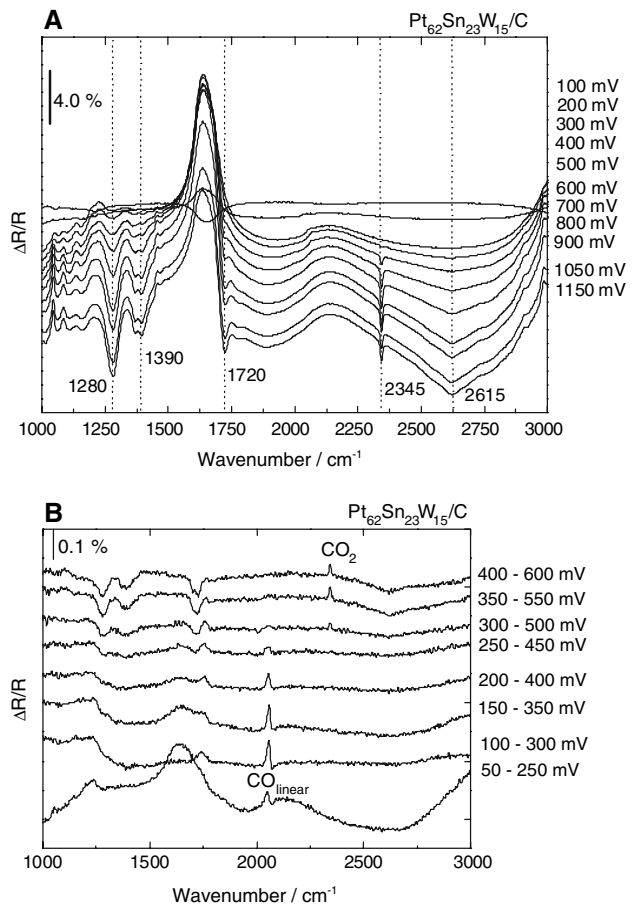

Fig. 5 (**a**) SPAIRS and (**b**) SNIFTIRS spectra of the species coming from ethanol (0.2 M) adsorption and oxidation, in 0.5 M H_2SO_4, on a $Pt_{62}Sn_{23}W_{15}/Au$ electrocatalyst at different potentials

1,720 cm^{-1} attributable to the carbonyl, C=O, stretching mode (ν_{CO}) is indicative of acetaldehyde and/or acetic acid produced from the ethanol oxidation reaction. The C–O stretching of acetic acid appears at 1,280 cm^{-1}, while the OH deformation from –COOH is at 1,390 cm^{-1} [8–10]. The presence of this molecule is also evidenced by the simultaneous appearance of the large band centered at 2,615 cm^{-1} (ν_{CH} of CH_3COOH). The band assigned to the formation of CO_2 is observed at 2,345 cm^{-1} for potentials higher than 0.3 V vs. RHE.

The band at 2,050 cm^{-1} (CO_L) is hardly detected by the SPAIRS technique in contrast to the SNIFTIRS technique used to obtain additional information. Figure 5b shows the representative SNIFTIR spectra obtained for ethanol oxidation on $Pt_{62}Sn_{23}W_{15}/Au$. The characteristic band of linearly adsorbed CO [8, 10] at ca. 2,050 cm^{-1} is clearly observed between 0.2 and 0.3 V vs. RHE, whereas that of CO_2 formation located at 2,345 cm^{-1} appears at potentials higher than 0.3 V vs. RHE, showing that the initial adsorption step of ethanol on the catalyst is a dissociative process.

Figure 6 shows intensities of IR bands obtained from *in situ* reflectance spectroscopy during ethanol oxidation on PtW/Au and PtSnW/Au. For the binary $Pt_{88}W_{12}$ and ternary $Pt_{62}Sn_{23}W_{15}$ catalysts, the CO_L intensity band increases between 0.05 and 0.15 V vs. RHE and thereafter decreases at potentials higher than 0.15 V vs. RHE. The formation of CO_2 occurs at potentials higher than 0.3 V for $Pt_{62}Sn_{23}W_{15}$ and 1.0 V for $Pt_{88}W_{12}$. In the case of $Pt_{85}Sn_8W_7$, the CO_L intensity band increases between 0.05 and 0.2 V *vs.* RHE and then decreases after potentials higher than 0.2 V vs. RHE. The CO_2 intensity band is visible at potentials higher than 0.1 V vs. RHE. This behavior is clearly related to the removal of CO_{ads} and/or CH_{xads} to form CO_2.

3.3 Fuel cell performance

Figure 7 shows the cell performance of Pt-based DEFC electrocatalysts employed as anodes. The open circuit

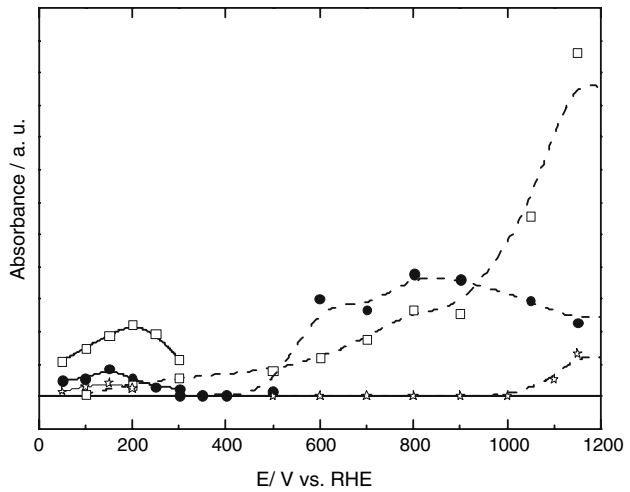

Fig. 6 Intensity of the CO_L (solid line) and CO_2 (dash line) bands as a function of the potential for different Pt-based electrocatalysts. (☆) $Pt_{88}W_{12}$/Au; (□) $Pt_{85}Sn_8W_7$/Au and (●) $Pt_{62}Sn_{23}W_{15}$/Au electrocatalysts. The intensities are taken from SNFTIR and SPAIR spectra of the species resulting from ethanol adsorption and oxidation: 0.5 M H_2SO_4 + 0.2 M ethanol

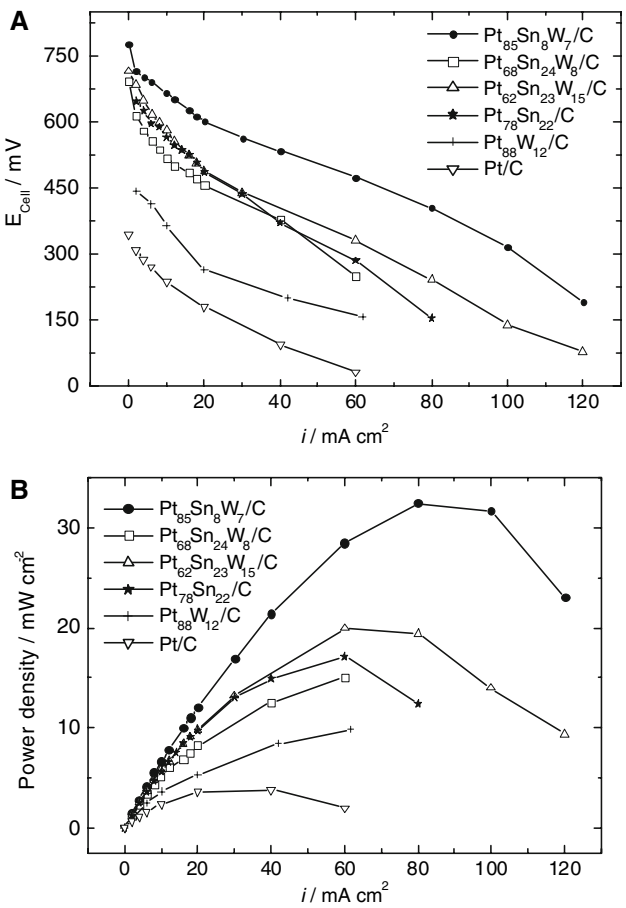

Fig. 7 Electrical performances of a 4.62 cm^2 DEFC at 90 °C using Pt-based bi and trimetallic anodes (1 mg cm^{-2} catalyst loading, 40 wt.% catalyst on carbon). P_{O_2} = 3 bar; P_{EtOH} = 1 bar; [EtOH] = 2.0 mol dm^{-3}; Nafion® 117 membrane. (**a**) Cell voltage–current density plots and (**b**) power density–current density plots

voltage of cells containing $Pt_{68}Sn_{24}W_8$/C and $Pt_{62}Sn_{23}W_{15}$/C catalysts are 0.70 and 0.72 V, respectively, while the corresponding value for the ternary $Pt_{85}Sn_8W_7$/C catalyst is ca. 0.78 V (Fig. 7a).

The DEFC performance obtained for the ternary $Pt_{85}Sn_8W_7$/C catalyst (33 mW cm^{-2}) is better than those of the $Pt_{68}Sn_{24}W_8$/C and $Pt_{62}Sn_{23}W_{15}$/C anodes (Fig. 7b). The higher activity of $Pt_{85}Sn_8W_7$/C at lower potentials, as observed in the CV and chronoamperometry experiments carried out at room temperature (cf. Figs. 3b and 4), is confirmed in the experiments in a single DEFC. As result, the power density obtained in this work remains higher than those reported in the literature under the same operating conditions [30, 32, 48].

4 Conclusions

Electrochemical characterizations of ternary PtSnW/C nanocatalysts synthesized by a DPP route show an enhancement of ethanol electrooxidation. The onset potential for this reaction was found to be 250 mV vs. RHE, which suggests that activation takes place at the electrode surface by a ligand effect. Additionally, the presence of Sn and W, under alloyed or bi- and trimetallic forms, favors the activation of interfacial water molecules, which is necessary for the removal of irreversibly adsorbed species such as linearly adsorbed CO at potentials lower than 300 mV. The latter species are well shown by in situ IR reflectance spectroscopy, which also allows the identification of acetaldehyde, acetic acid and carbon dioxide as the reaction products, detected in parallel by chromatography. The physico-chemical measurements of the catalysts (TEM) show that the particles sizes decrease from binary to ternary compositions of the catalysts. This decrease in particles size for ternary electrocatalysts leads to an additional promotion, as the consequence of the modification of the adsorption properties of such small particles (structural effect, but also bi-functional mechanism). The $Pt_{85}Sn_8W_7$/C catalyst used here as anode improves the open circuit voltage and the maximum power density of a single DEFC (0.78 V and 33 mW cm^{-2}, respectively) when compared to those obtained with Pt, PtSn catalysts under the same operating conditions.

Acknowledgements This work was mainly conducted within the framework of a collaborative program CAPES/COFECUB under grant n°498/05. J. Ribeiro acknowledges CAPES for the postdoc fellowship (BEX n° 0006/06-8). G. Tremiliosi-Filho, P. Olivi and A. R. de Andrade acknowledge FAPESP, FINEP and CNPq (Brazil).

References

1. Vigier F, Coutanceau C, Hahn F, Belgsir EM, Lamy C (2004) J Electroanal Chem 563:81
2. Lamy C (2006) In: Lens PNL, Kennes C, Le Cloirec P, Deshusses MA (eds) Waste gas treatment for resource recovery, integrated environmental technology series, Chap. 21. IWA publishing, pp 360–383
3. Iwasita T, Pastor E (1994) Electrochim Acta 39:531
4. Xia XH, Liess H-D, Iwasita T (1997) J Electroanal Chem 437:233
5. Neto AO, Giz MJ, Perez J, Ticianelli EA, Gonzalez ER (2002) J Electrochem Soc 149:A272
6. Camara GA, de Lima RB, Iwasita T (2004) Electrochem Commun 6:812
7. Shao MH, Adzic RR (2005) Electrochim Acta 50:2415
8. Lamy C, Belgsir EM, Léger J-M (2001) J Appl Electrochem 31:799
9. Camara GA, de Lima RB, Iwasita T (2005) J Electroanal Chem 585:128
10. Léger J-M, Rousseau S, Coutanceau C, Hahn F, Lamy C (2005) Electrochim Acta 50:5118
11. Jusys Z, Schmidt TJ, Dubau L, Lasch K, Jörissen L, Garche J, Behm RJ (2002) J Power Sources 105:297
12. Santos VP, Tremiliosi-Filho G (2003) J Electroanal Chem 554–555:395
13. Pereira MG, Jiménez MD, Elizalde MP, Manzo-Robledo A, Alonso-Vante N (2004) Electrochim Acta 49:3917
14. Zhou WJ, Song SQ, Li WZ, Sun GQ, Xin Q, Kontou S, Poulianitis K, Tsiakaras P (2004) Solid State Ionics 175:797
15. Xu C, Shen PK, Ji X, Zeng R, Liu Y (2005) Electrochem Commun 7:1305
16. Tarasevich MR, Karichev ZR, Bogdanovskaya VA, Lubnin EN, Kapustin AV (2005) Electrochem Commun 7:141
17. Jiang L, Sun G, Sun S, Liu J, Tang S, Li H, Zhou B, Xin Q (2005) Electrochim Acta 50:5384
18. Song SQ, Zhou WJ, Zhou ZH, Jiang LH, Sun GQ, Xin Q, Leontidis V, Kontou S, Tsiakaras P (2005) Int J Hydrogen Energy 30:995
19. Zhou WJ, Song SQ, Li WZ, Zhou ZH, Sun GQ, Xin Q, Douvartzides S, Tsiakaras P (2005) J Power Sources 140:50
20. Wang H, Jusys Z, Behm RJ (2006) J Power Sources 154:351
21. Mann J, Yao N, Bocarsly AB (2006) Langmuir 22:10432
22. Colmenares L, Wang H, Jusys Z, Jiang L, Yan S, Sun GQ, Behm RJ (2006) Electrochim Acta 52:221
23. Goetz M, Wendt H (1998) Electrochim Acta 43:3637
24. Neto AO, Perez J, Napporn WT, Ticianelli EA, Gonzalez ER (2000) J Braz Chem Soc 11:39
25. Roth C, Goetz M, Fuess H (2001) J Appl Electrochem 31:793
26. de Oliveira MB, Profeti LPR, Olivi P (2005) Electrochem Commun 7:703
27. dos Anjos DM, Kokoh KB, Léger J-M, de Andrade AR, Olivi P, Tremiliosi-Filho G (2006) J Appl Electrochem 36:1391
28. Ribeiro J, dos Anjos DM, Kokoh KB, Coutanceau C, Léger J-M, Olivi P, de Andrade AR, Tremiliosi-Filho G (2007) Electrochim Acta 52:6997
29. Lamy C, Rousseau S, Belgsir EM, Coutanceau C, Léger J-M (2004) Electrochim Acta 49:3901
30. Rousseau S, Coutanceau C, Lamy C, Léger J-M (2006) J Power Sources 158:18
31. Antolini E, Colmati F, Gonzalez ER (2007) Electrochem Commun 9:398
32. Colmati F, Antolini E, Gonzalez ER (2007) J Electrochem Soc 154:B39
33. Zhou W, Zhou Z, Song S, Li W, Sun G, Tsiakaras P, Xin Q (2003) Appl Catal B: Environ 46:273
34. Roman-Martinez C, Cazorla-Amoros D, Yamashita H, de Miguel S, Scelza OA (2000) Langmuir 16:1123
35. Li H, Sun G, Cao L, Jiang L, Xin Q (2007) Electrochim Acta 52:6622
36. Umeda M, Ojima H, Mohamedi M, Uchida I (2004) J Power Sources 136:10
37. Shen PK, Tseung ACC (1994) J Electrochem Soc 141:3082
38. Tanaka S, Umeda M, Ojima H, Usui Y, Kimura O, Uchida I (2005) J Power Sources 152:34
39. McLeod EJ, Birss VI (2005) Electrochim Acta 51:684
40. Profeti LPR, Simões FC, Olivi P, Kokoh KB, Coutanceau C, Léger J-M, Lamy C (2006) J Power Sources 158:1195
41. Pechini MP, Adams N (1967) US Patent, 3,330,697:1
42. Ribeiro J, Alves PDP, de Andrade AR (2007) J Mater Sci 42:9293
43. Cullity BD (1978) In: Elements of X-Ray diffraction. Addison-Wesley, San Francisco, p. 102
44. Powder Diffraction File: 01-087-0646, 00-035-1360 and 00-041-0905 Joint Committee on Powder Diffraction Standards (2005) International Center for Diffraction Data, Vol. PDF-2, Pennsylvania, USA
45. Sutton LE (1965) In: Table of interatomic distances and configuration in molecules and ions, Supplement 1956–1959, Special publication No. 18, Chemical Society, London, UK
46. Hume-Rothery W, Smallman RE, Hayworth CW (1969) The structure of metals and alloy, London
47. Ribeiro J, de Andrade AR (2004) J Electrochem Soc 151:D106
48. Colmati F, Antolini E, Gonzalez ER (2007) Appl Catal B: Environ 73:106
49. Calegaro ML, Suffredini HB, Machado SAS, Avaca LA (2006) J Power Sources 156:300
50. Vielstich W (1968) In: Fuel cells: modern processes for the electrochemical production of energy, Wiley-Interscience
51. Lamy C, Lima A, Le Rhun V, Delime F, Coutanceau C, Léger J-M (2002) J Power Sources 105:283